# Investigation of Compensated Foundation Settlement Mechanism Based on FEM-DEM Coupling Method

Xiaoyong Zhang[1], Linhai Lv[2], Meijuan Xu[3] and Guoxiong Mei[4,*]

[1] Department of Architectural Engineering, Guizhou Communications Polytechnic University, Guiyang, 551400, China

[2] College of Civil Engineering and Architecture, Guangxi University, Nanning, 530004, China

[3] Department of Civil Engineering, Hangzhou City University, Hangzhou, 310000, China

[4] Ocean College, Zhejiang University, Zhoushan, 316000, China


**INFORMATION**

**Keywords:**
Compensated foundations
FEM-DEM
rigid retaining wall
force chain
over-excavation

**DOI:** 10.23967/j.rimni.2025.10.71075

SCIPEDIA Revista Internacional de Métodos Numéricos para Cálculo y Diseño en Ingeniería

Revista Internacional Métodos numéricos para cálculo y diseño en ingeniería RIMNI in cooperation with CIMNE

# Investigation of Compensated Foundation Settlement Mechanism Based on FEM-DEM Coupling Method

**Xiaoyong Zhang[1], Linhai Lv[2], Meijuan Xu[3] and Guoxiong Mei[4,*]**

[1]Department of Architectural Engineering, Guizhou Communications Polytechnic University, Guiyang, 551400, China

[2]College of Civil Engineering and Architecture, Guangxi University, Nanning, 530004, China

[3]Department of Civil Engineering, Hangzhou City University, Hangzhou, 310000, China

[4]Ocean College, Zhejiang University, Zhoushan, 316000, China

**ABSTRACT**

The application of compensated foundations is common in engineering, but significant settlements often occur during the application process. A foundation pit model supported by a rigid retaining wall was established based on the Finite Element Method-Discrete Element Method (FEM-DEM), and a cantilevered layer-by-layer excavation process was simulated. A rolling resistance linear model was used to simulate the sand, while a variable particle size method was adopted to establish the foundation model. It is shown that during the excavation process of the foundation pit, the stress of the sand at the pit bottom gradually decreases, and the displacement of the soil changes gradually from settlement to uplift as one moves from behind the retaining wall to the bottom of the foundation pit. Moreover, the porosity of the sand at the pit bottom gradually increases. As a result, the strength of the uplifted sand at the pit bottom decreases due to over-excavation during the foundation pit excavation stage. The uplifted sand is finally excavated during the site leveling stage, resulting in a further decrease in the strength of the sand at the pit bottom. Finally, an inverted arch bottom plate structure is proposed to mitigate the over-excavation settlement of the compensated foundation.

**OPEN ACCESS**

**Received:** 31/07/2025

**Accepted:** 03/11/2025

**Published:** 23/01/2026

**DOI**
10.23967/j.rimni.2025.10.71075

**Keywords:**
Compensated foundations
FEM-DEM
rigid retaining wall
force chain
over-excavation

## 1 Introduction

With the increasing attention to the development and utilization of underground space, compensated foundations have also been applied more and more widely [1–3]. Compensated foundations are commonly used for deep foundation pits, in which the effective stress at the pit bottom is enough to partially or fully overcome the applied load. In other words, the unloading caused by excavation equals or exceeds the weight of the upper structure [4,5]. The structures on the compensated foundations will not settle in principle, and sometimes they even uplift. A simplified analysis method for compensated foundations was proposed by Sales et al. (2010) [6], and they suggested that the analysis of the design method of this kind of foundation should be combined with the measurement and prediction results. Four types of deformation of compensated foundations are found according to the case of super high-rise buildings in Shanghai soft soil foundation: uplift caused by excavation, recompression caused

*Correspondence: Guoxiong Mei (meiguox@163.com). 

by constant load, recompression caused by live load and settlement over time [6]. However, large settlements of compensated foundations are often encountered in practical engineering. For example, a settlement of 96 mm occurred under the over-compensation condition during the construction of Nanjing Metro Line 1, and the stable trend was not clear, so the foundation needed to be re-strengthened [7–9]. Therefore, the change law of the soil under the compensated foundation after the foundation pit excavation needs to be further studied.

The foundation pit is generally excavated from top to bottom, and the stress and strain state of the soil below the foundation pit bottom will undergo significant changes in this process. Retaining structures are generally used to restrain the soil around the foundation pit during the excavation process, and the soil at the foundation pit bottom bears unloading in the vertical direction [4]. As shown in Fig. 1, the stress distribution of the soil after the foundation pit excavation is completed, and the base will uplift due to the stress release of the soil at the bottom of the foundation pit. In addition, the tension zone ($P_c = \gamma \times D$) in the soil appears below the foundation pit bottom, and it decreases with the depth increasing.

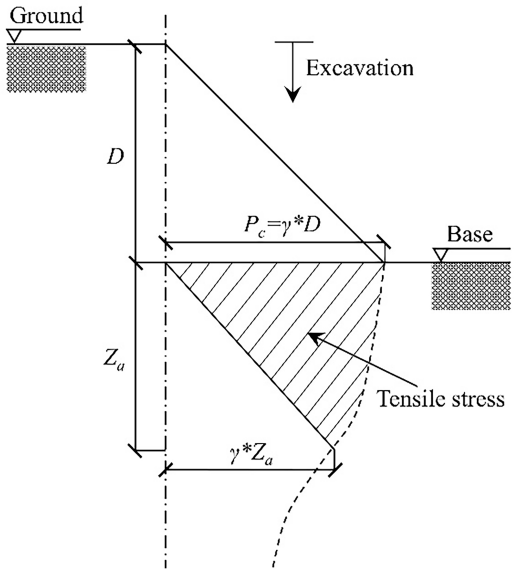


**Figure 1:** Stress distribution within the soil after excavation

Theoretically, in the process of foundation pit construction, the uplift amount of the soil at the foundation pit bottom is always kept constant, then as the foundation and upper structure are constructed, the soil will gradually enter the recompression stage, and also approximate to the characteristics before the foundation pit excavation. If the foundation is fully compensated or over-compensated, the unloading amount is enough to counteract the load of the upper structure, and additional settlement will not occur in the recompression stage [10,11].

However, this is an ideal situation. In practice, for the purpose of construction convenience and achieving a level foundation pit bottom, the excavated soil at the bottom of the pit is usually removed. In this case, when the soil undergoes recompression due to constant and variable loads, settlement is likely to occur since the applied load exceeds the relieved pressure (i.e., the effective stress). The schematic diagram of over-excavation resulting from the base uplift is shown in Fig. 2. The upper concave contour of the base represents the height of the pit uplift. The construction

excavation actually corresponds to an over-excavation, transforming the originally uniform soil layer into an uneven medium. The soil mass on the side wall of the foundation pit becomes denser, while it is looser in the middle, and the strength of the soil mass is significantly weakened. Therefore, the compensated foundation will encounter greater settlement in actual engineering. Building houses on such over-excavated foundation soil will not only lead to increased settlement of the building, but also significantly increase the internal force of the foundation slab.

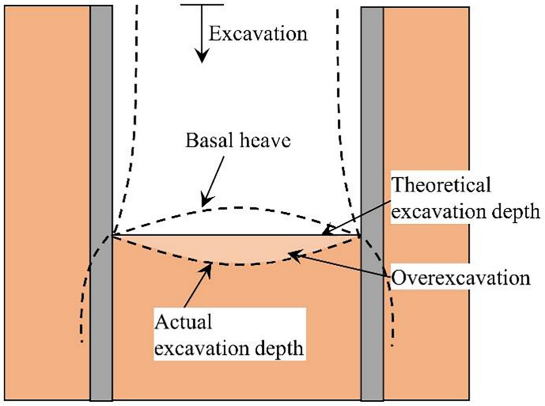


**Figure 2:** Schematics of over-excavation due to basal heave

The DEM provides an effective approach for analyzing large deformations and discontinuity problems in geotechnical engineering [12]. DEM has the unique advantage of capturing the motion behavior of discrete media and has been widely utilized to investigate the micro-behavior of granular materials [13–15]. Therefore, DEM is regarded as a robust supplement to laboratory experiments and the FEM [16,17]. In recent years, scholars have used the DEM to study foundation pit excavation. Lo [18] used the PFC2D to simulate the variation of internal forces and soil displacement during foundation pit excavation with flexible support structures. Peng [19] used the discrete element method to simulate the deformation mechanisms of different types of flexible retaining walls in sandy soil, while Jia et al. [20] analyzed soil deformation during excavation using the discrete element method. Widuliński et al. [21] investigated the soil pressure pattern of retaining walls based on the rotational resistance between particles and found that particle rotational resistance can increase the peak and residual strengths of soil. Jiang et al. [22] considered the twisting force in the particle micro-contact model to study the passive soil pressure of a rigid retaining wall and revealed the influence of particle rotational resistance on the magnitude and distribution of soil pressure behind the wall. Based on the above analysis, it can be observed that the DEM excels in simulating soil failure, post-failure large deformation problems, as well as microscopic variations that are challenging to measure in actual engineering scenarios. While the DEM is currently not suitable for practical engineering design, its analysis results on the excavation process mechanisms of foundation pits have guiding significance. Therefore, studying the excavation process of foundation pits using the DEM will help to gain a more profound understanding of the settlement mechanisms in compensated foundations.

The development of the FEM-DEM coupled method, pioneered by Nakashima and Oida [23], was driven by the need to integrate the advantages of different modeling schemes while minimizing computational demands, initially for analyzing soil-tire interaction. This hybrid methodology has since seen progressively wider adoption in geotechnical engineering. It has been successfully applied to diverse challenges, such as investigating the acoustic emission (AE) mechanisms during excavation [24],

studying the stability effects of blast-induced damage zones (BIDZ) [25], and simulating tunnel-soil vibrations under train loads [26].

Building on the versatility of this established framework, our study applies it to the specific problem of compensated foundations. While conventional continuum models can capture macroscopic deformation, their inherent homogenization of the soil mass prevents a deeper understanding of the fundamental particle-scale mechanics. In contrast, the DEM provides a direct pathway to revealing these core mechanisms by tracking the mechanical behavior of each particle. This allows for the clear observation of microscopic phenomena such as the evolution of the force chain network, dynamic changes in the pore structure, and the kinematic behavior of particles. To balance computational efficiency with physical realism, a hybrid strategy is employed: the computationally efficient FEM is used for the continuum structure (the retaining wall), while the physically insightful DEM is used for the granular medium (the soil). The FEM-DEM coupled approach is therefore selected as the optimal tool for this investigation, as it harnesses the respective strengths of both techniques to tackle this complex soil-structure interaction challenge.

In summary, this study utilized the FEM-DEM method to simulate the cantilever excavation process of a three-dimensional gravity retaining wall system, aiming to investigate the settlement mechanisms of compensated foundations. Firstly, the sand was modeled using the rotational resistance linear contact model (rrlinear). The microscopic parameters of the sand were calibrated based on triaxial compression simulations with flexible boundaries. Furthermore, a DEM model of excavation in a foundation pit was established using the variable particle size method. Finally, a comprehensive analysis of the numerical simulation results was carried out to derive the settlement mechanisms of compensated foundations from stress fields, displacement fields, force chains, and energy fields.

## 2 Establishment of the Discrete Element Model

### *2.1 Basic Information for the Model of the Foundation Pit*

The cantilever excavation process of a foundation pit supported by gravity retaining walls is simulated in this paper using DEM. The excavation of the actual foundation pit has a width of 20 m, depth of 10 m, radius of 20 m, and a retaining wall thickness of 1.2 m. The retaining wall extends 20 m below the excavation face [27]. Considering the spatial symmetry of foundation pit excavation, 1/4 of the actual foundation pit is taken as the research object. And the horizontal and vertical dimensions of the soil model are taken as 8 times and 6 times the excavation depth, respectively, to avoid the influence of size effects on the results. Following the principles of similarity [28,29], a size similarity ratio of 20 is chosen. The dimensions of the prototype excavation are reduced by a factor of 20, while a 20-fold gravity acceleration is applied to simulate the self-weight stress field of the prototype. Specific dimensions of the model are presented in Fig. 3.

### *2.2 Selection of Contact Models*

The rolling resistance model was employed in this study to approximate the mechanical behavior of non-spherical sand particles. This model simulates the energy dissipation and rotational constraints caused by irregular particle shapes by introducing an additional torque at contact points that opposes rotation. However, it should be noted that this is a simplification. The model cannot fully replicate the complex geometric interlocking and multi-point contact phenomena that arise from the intricate shapes of real, highly angular or elongated particles. Consequently, for materials with very high angularity, the model may underestimate the shear strength or dilatancy that is heavily dependent on such interlocking.

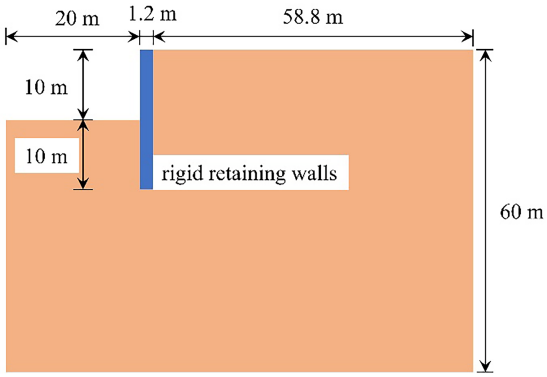


**Figure 3:** Schematic diagram for dimensions of foundation pit excavation model

Fujian Standard Sand is adopted as the simulated material in this study [30], which is a commonly used material in the investigation of sandy soil-related issues and finds extensive applications in model experiments and unit tests. The scanning electron microscope image of the sand reveals a "subangular" shape, as depicted in Fig. 4 [31]. However, in discrete element method simulations, sand particles are often simplified as discs (2D) or spheres (3D), failing to capture the actual particle shape and interlocking behavior. The essence of the particle's resistance to rotation is a mechanical effect caused by the irregular shape of soil or sand particles. It also serves as a significant source of shear strength, as illustrated in Fig. 5. In order to analyze the impact of the actual shape of particles, studies by Iwashita and Oda [32] have indicated the significant influence of inter-particle resistance to rotation on the strength and dilation characteristics of sand. Similarly, Jiang et al. [33] studied the mechanical response of rough particles using DEM, while Mohamed and Gutierrez [34] explained the important influence of the resistance to rotation of particle material on the formation of shear bands. Thus, in order to consider the shape effect of sand, this study employs the Rolling Resistance Linear Model (rrlinear) to establish the excavation model for the foundation pit. Additionally, the contact model available in DEM is based on a linear model that incorporates a torque to counteract rolling motion [35]. In contrast to the linear contact model, the rrlinear contact model includes a rotational contact component in addition to the normal and tangential contact components. This study utilizes Fujian Standard Sand, a uniform reference material chosen to ensure the repeatability of the results. However, natural field soils are typically more complex and heterogeneous. Consequently, while this study reveals fundamental physical mechanisms, the direct application of its quantitative results (e.g., specific settlement values) to a field site would require site-specific material characterization and model calibration.

$$M_{RR} = k_r \Delta\varphi_r \tag{1}$$

$$k_r = k_s \left[ \frac{R_1 R_2}{(R_1 + R_2)} \right]^2 \tag{2}$$

where $M_{RR}$ represents the rolling resistance torque, $\Delta\varphi_r$ represents the relative rotation increment between the contacting particles, $k_r$ and $k_s$ represent the relative rotation increments between the contacting particles, and $R_1$ and $R_2$ are the radii of the two contacting particles [36].

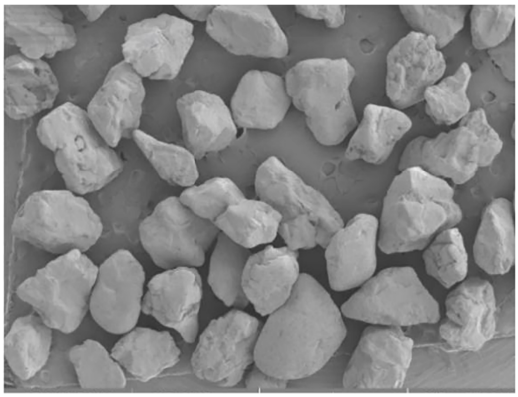

**Figure 4:** SEM picture of Fujian sand

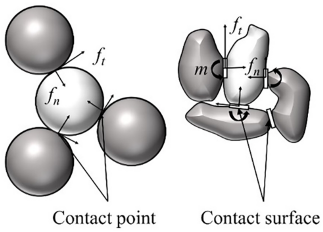


**Figure 5:** Origin of rolling resistance at contact

The principle of FEM-DEM coupling is illustrated in Fig. 6. This approach uses walls/shells as interaction interfaces. Velocity data from the continuous element nodes are passed to the wall/shell unit nodes, where they are converted into unbalanced forces, which are then distributed to the DEM particles via shape functions. Likewise, the unbalanced forces in the DEM are converted into velocity and sent back to the continuous element nodes through the wall/shell unit nodes, continuing the cycle until dynamic equilibrium is reached. Once coupling is activated, the calculation must run under large deformation conditions, and to ensure the balance of forces and moments at the coupling interface, full computation mode should be activated [37].

### *2.3 Parameter Calibration*

The sand used in this study is Fujian standard sand, which is a common material for investigating sand-related issues and is widely used in model tests and element tests [21]. Conventional physical and mechanical tests were conducted on the standard sand in accordance with the "Standard for Geotechnical Testing Method" (GB/T 50123-2019), and its main physical properties are shown in Table 1. The non-uniformity coefficient ($C_u$) of the standard sand is 5.774, the coefficient of curvature ($C_c$) is 1.458, and the mean particle size ($d_{50}$) is 0.524 mm. This indicates that the sand used in the test is a well-graded medium sand.

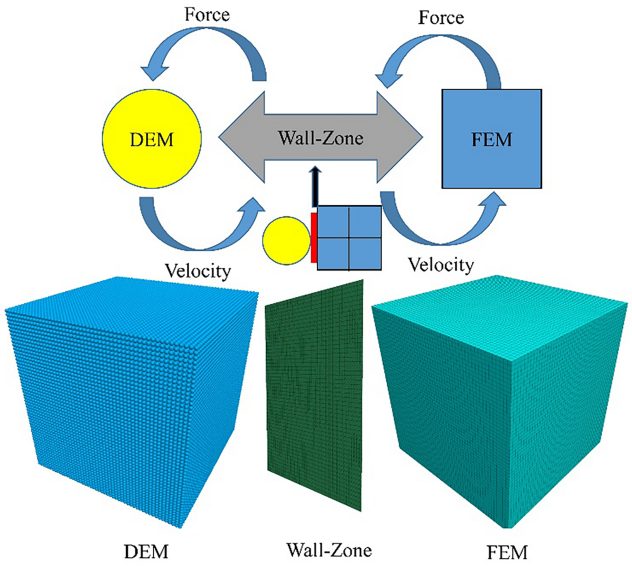


**Figure 6:** The principle of FEM-DEM coupling

**Table 1:** Physical parameters of standard sand

| Initial dry density $\rho_d$ (g/cm$^3$) | Maximum dry density $\rho_{dmax}$ (g/cm$^3$) | Minimum dry density $\rho_{dmin}$ (g/cm$^3$) | Specific gravity $G_s$ |
|---|---|---|---|
| 1.630 | 1.740 | 1.416 | 2.643 |

To calibrate the microscale parameters of Fujian sand, laboratory drained triaxial tests were conducted, and a corresponding numerical model for flexible triaxial compression was developed using the FEM-DEM coupling method (see Fig. 7). The sand sample has a diameter of 30 mm and a height of 60 mm, prepared using the dry deposition method. Under drained conditions, the sample is saturated and subjected to shear at a constant rate of $\varepsilon_a = 0.04\%/\text{min}$ (where $\varepsilon_a$ represents the axial strain) under a confining pressure of 100 kPa. In the corresponding discrete element numerical modeling, a cylindrical specimen is first created with the same gradation as the core region. The dimensions of the specimen are consistent with the laboratory triaxial test, with rigid loading plates on the top and bottom surfaces having the same stiffness as the particles. The side walls are modeled as flexible constraints using shell elements from finite elements [38], with an elastic modulus of $1 \times 10^6$ Pa, Poisson's ratio of 0.25, thickness of 0.25 mm, and a boundary wall friction coefficient of 0, with the relevant parameters derived from the flexible membrane used in the laboratory test. The servo control system performs isotropic consolidation by inducing relative motion between the upper and lower loading plates, with very slow plate velocities to simulate quasi-static loading [39]. The Fish function is utilized to automatically adjust the stress on the side walls, ensuring a constant confining pressure. The confining pressure error is strictly controlled to be below 1% throughout the loading process until the axial strain reaches 10%, at which point the loading process is halted [40].

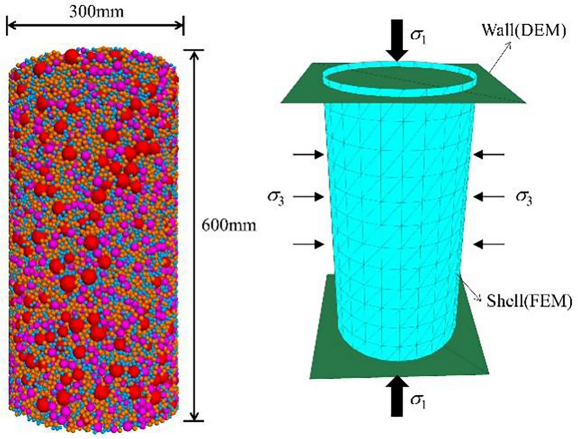


**Figure 7:** Numerical model of FEM-DEM triaxial test

Fig. 8 shows the results of the micro-parameter calibration for the discrete element triaxial compression test. The simulated deviatoric stress-strain curve is in good agreement with the curve from the laboratory test, indicating that the flexible triaxial simulation can reflect the physical and mechanical properties of sand from a micro-scale perspective. The final internal friction angle obtained from the DEM simulation is 37.44°, which is close to the laboratory test result of 38.33° (an error of approximately 2.3%). Therefore, these micro-parameters can be used for subsequent DEM simulations.

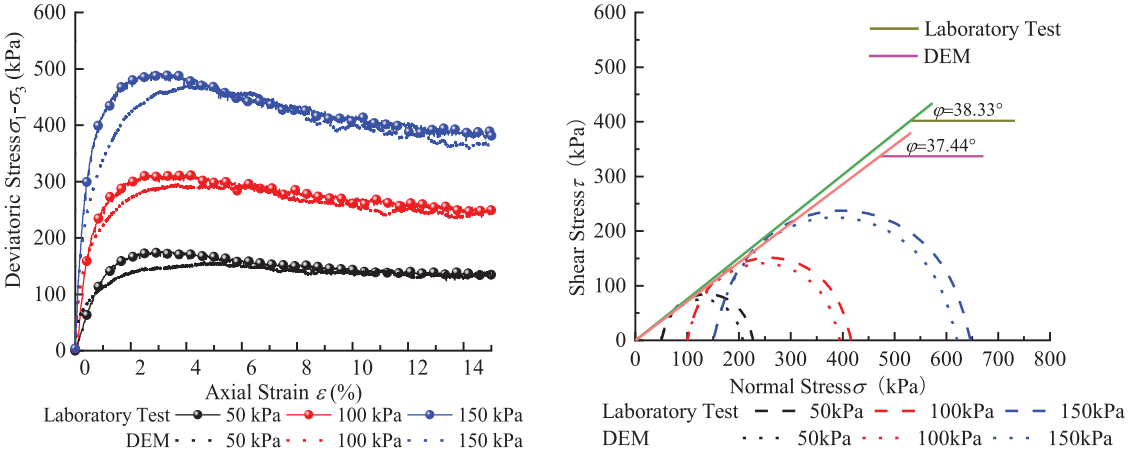


(**a**) Deviatoric stress—axial strain curve (**b**) Mohr's stress circle

**Figure 8:** Calibration results of DEM micro-parameters for standard sand

### *2.4 Sample Preparation*

To reduce the particle count and enhance computational efficiency, this study employs the variable particle-size method to construct the discrete element model, referencing the works of McDowell et al. [41] and Deng et al. [42]. The principle is shown in Fig. 9, and the specific steps are as follows: (1) The discrete element model is divided into multiple zones, labeled as $Z_1$, $Z_2$, ..., $Z_n$, ranging from the near-field to the far-field. Small-sized particles are used in the core zone of the near-field to

simulate its complex physical and mechanical characteristics. (2) The particle size gradually increases in the other zones to simulate the boundary regions. The zones outside the core region are less affected by the excavation disturbance, allowing for larger particle sizes to ensure computational efficiency. Additionally, mixed zones ($M_{12}$, $M_{23}$, ..., $M_{(n-1)n}$) are introduced between adjacent variable particle-size zones to prevent particle interlocking at the interface. The mixed zone consists of a combination of the two particle sizes from the adjacent zones, maintaining the same compaction level as the neighboring zones.

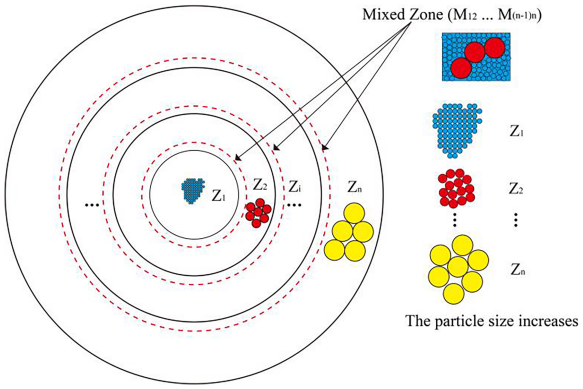


**Figure 9:** Schematic diagram of the variable particle-size modeling method

The validity of this approach has been verified through a series of numerical tests. The work by Deng et al. [42] demonstrated that samples with different particle sizes adhering to this scaling law exhibit nearly identical stress-strain and volumetric strain responses in numerical triaxial tests. Furthermore, their Cone Penetration Test (CPT) simulations also showed that the results from the variable-size model were in excellent agreement with those from a reference model using uniformly fine particles. Therefore, by adopting this rigorously validated modeling method, this study minimizes the potential deviation in mechanical response that could be introduced by using enlarged particles, ensuring the reliability of the simulation results.

The process of applying the variable particle-size method in this paper is as follows: Determine the particle size and its range for the core zone $Z_1$. After extensive calculations, the particle size for the core zone is determined to be in the range of 23.76–47.52 mm, with a $d_{50} = 40$ mm, and the length of the zone is set to 1.5 m. Fig. 10 compares the particle size distribution (PSD) of the Fujian sand sample with the particles in the core zone. The uniformity coefficient ($C_u$) and curvature coefficient ($C_c$) of Fujian sand are 1.542 and 1.104, respectively. These values are highly similar to the uniformity coefficient ($C_u$) and curvature coefficient ($C_c$) of the DEM particles used in the core zone, which are 1.51 and 1.12, respectively. And the particle sizes in the intermediate region $Z_2$ and the boundary region $Z_3$ are 1.5 times (60 mm) and 2 times (80 mm) larger than the median particle size of the core particles. The particle size distribution in the mixed region is taken from the particle sizes of the two adjacent regions, with the median particle size taken for the core region. The particle sizes in the two mixed regions are $M_{12}$ (0.04–0.06 m) and $M_{23}$ (0.06–0.08 m), respectively. Despite the fact that the smallest particles described in this study are larger than the largest sand particles in reality, this deviation from reality is necessary in order to reduce computational costs [43,44].

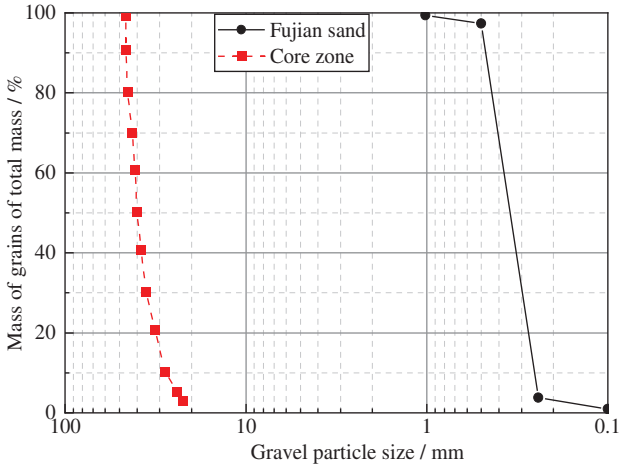


**Figure 10:** Comparison of particle size distribution between Fujian sand and the numerical sample

Additionally, due to the enlargement of particle sizes, it is necessary to adjust the microscale parameters according to the scaling relationship to ensure consistency in the corresponding physical and mechanical properties of different zones. Therefore, by maintaining the ratio of particle normal contact stiffness ($k_n$) to the average particle size (d), the particle stiffness can be optimized, approximately satisfying macroscopic elastic consistency [45]. The core zone uses the ratio between median particle sizes as the reference. The wall stiffness is consistent with the particle stiffness in the core zone, and the friction coefficient is set to zero to eliminate the effect of wall friction. The resulting particle radius range and microscopic parameters are shown in Table 2.

**Table 2:** Microscopic parameters of the foundation model

| Parameter assigment | Contact model | Group | Particles radius (mm) | Particle position range (m) | Density of particles (kg/m) | Normal stiffness (N/m) | Shear stiffness (N/m) | Friction coefficient | Rolling friction coefficient (MN · m) |
|---|---|---|---|---|---|---|---|---|---|
| Backfill | RRlinear | $Z_1$ | 23.76–47.52 ($d_{50} = 40$) | 0–1.5 | 2650 | $1 \times 10^8$ | $1 \times 10^8$ | 0.3 | 0.2 |
| | | $M_{12}$ | 40–60 | 1.5–2 | | 1.5 | 1.5 | | |
| | | $Z_2$ | 60 | 2–2.5 | | 2 | 2 | | |
| | | $M_{23}$ | 60–80 | 2.5–3 | | 3 | 3 | | |
| | | $Z_3$ | 80 | 3–4 | | 4 | 4 | | |

In the model, the interface friction coefficient between the soil particles and the FEM retaining wall was set to 0.3. This value was selected based on typical friction characteristics for sand-concrete interfaces found in geotechnical literature and is consistent with the inter-particle friction coefficient of 0.3 used for the backfill soil in this study. This parameter is critical for accurately simulating the soil-structure interaction, as it directly governs the shear stress transfer between the soil mass and the wall, thereby influencing the distribution of earth pressure acting on the wall and the settlement patterns of the ground surface behind it.

$\overline{k}_n = \lambda k_n, \overline{k}_s = \lambda k_s$

where $\lambda$ is the particle size enlargement factor, $k_n$ and $k_s$ are the normal stiffness and shear stiffness, respectively, between two particles.

The process of generating the model is as follows [46,47]: (1) The discrete element model of the foundation is generated using the variable particle-size method (Fig. 11a); (2) Multiple iterations are performed to eliminate the imbalanced forces between particles during the model construction process. Subsequently, the rigid walls between different regions are removed, and the imbalanced forces between the regions are re-equilibrated (Fig. 11b); (3) The model's gravitational acceleration is gradually increased to 20 g (196 m/s$^2$) following the principle of a centrifuge. The entire equilibrium process is divided into 20 levels, with each level applying double the gravity acceleration of the previous level. Sufficient time steps are performed for each level until settlement stabilizes before proceeding to the next level. The final simulation represents the actual ground stress level equivalent to a depth of 80 m $\times$ 60 m (under 20 g gravitational acceleration). Additionally, the top walls are removed to simulate a free top boundary (Fig. 11c); (4) Establish the model of a supported retaining wall. Remove the particles at the location of the retaining wall and use the "zone" command to generate the wall structure in that position. Simultaneously, apply the "fix" command to restrict the deformation of the retaining wall. After the completion of the model, reestablish equilibrium under the influence of 20 g gravitational acceleration. The DEM-FEM coupling method was used to establish the contact surface between the particles and the finite element retaining wall surface (Fig. 11d). This method enables the investigation of deformation and failure mechanisms in soil and rock masses while maintaining a higher level of computational efficiency.

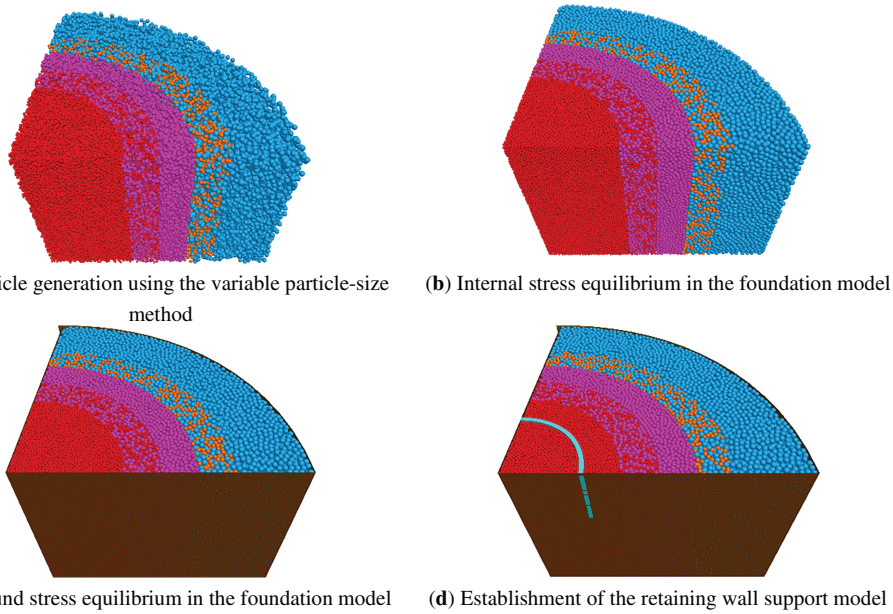

(**a**) Particle generation using the variable particle-size method

(**b**) Internal stress equilibrium in the foundation model

(**c**) Ground stress equilibrium in the foundation model

(**d**) Establishment of the retaining wall support model

**Figure 11:** The process of establishing the excavation model of the foundation pit

The model parameters of the retaining wall are based on the elastic modulus of 25 GPa, Poisson's ratio of 0.15, and density of 2500 kg/m$^3$ as presented in reference [40] (see Table 3). The resulting discrete element method of the foundation pit is shown in Fig. 12.

**Table 3:** Finite element parameters of the retaining wall

| FEM | Model | Density ($kg/m^3$) | Young's modulus (GPa) | Poisson's ratio (GPa) | Bulk modulus (GPa) | Shear modulus (GPa) |
|---|---|---|---|---|---|---|
| Retaining wall | Linear elastic model | 2500 | 25 | 0.15 | 13.9 | 10.4 |

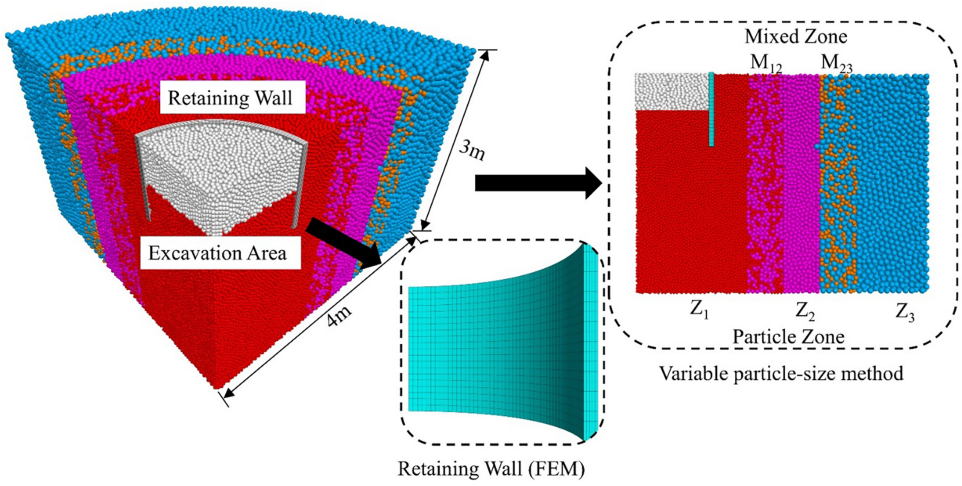


**Figure 12:** Schematic diagram of discrete element model

A 1/4 symmetry model was adopted in this study to significantly reduce the high computational cost associated with the three-dimensional discrete element simulation. This simplification is justified by the axisymmetric geometry of the circular foundation pit being modeled. By modeling only one-quarter of the domain, the computational efficiency was substantially increased, allowing for a higher resolution in the zone of interest. However, it should be acknowledged that this assumption of symmetry precludes the analysis of any potential asymmetric deformation modes that could arise from local material heterogeneities or non-symmetric construction loads.

The numerical simulations in this study were conducted on a high-performance workstation equipped with an AMD R7-9700X processor (8-core, 16-thread, 3.80–5.50 GHz). For the three-dimensional FEM-DEM coupled model presented, the approximate time required to complete a single full simulation, from sample generation through all excavation steps, was approximately 36 h. This significant computational cost was the primary constraint that precluded more extensive analyses, such as a full parametric sensitivity study or multiple realizations for an uncertainty analysis, within the scope of the current work.

The numerical simulation workflow adopted in this study is summarized in Fig. 13, which consists of four main stages.

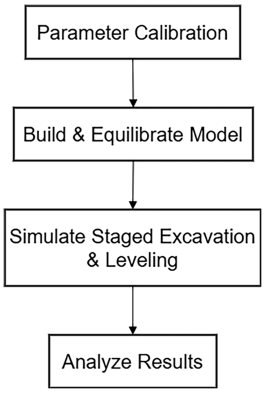


**Figure 13:** The numerical simulation workflow

### *2.5 Assessment of the Discrete Element Foundation Modell*

Fig. 14 illustrates the displacement and force chain distribution of the model after gravity deposition. It can be observed that the settlement displacement is horizontally distributed, and the force chains exhibit a dense distribution in the lower part and a loose distribution in the upper part, which is consistent with the actual distribution pattern. The initial porosity, static earth pressure coefficient $K_0$, and vertical and horizontal stress distributions under the influence of gravity are shown in Fig. 15. It can be seen from the figure that, under the action of gravity, the porosity of the soil fluctuates around 0.4 with depth. The static earth pressure coefficient $K_0'$ is close to the theoretical value. The horizontal stress and vertical stress change linearly with depth, and their values are basically consistent with the calculated values by $\sigma_v = \gamma h$ and $\sigma_h = K_0 \gamma h$.

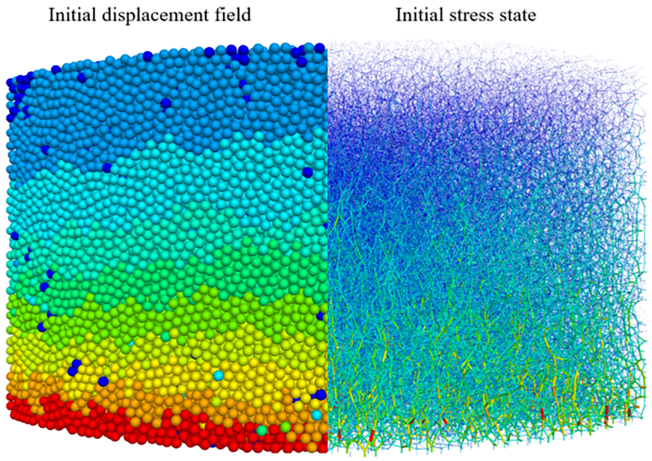


**Figure 14:** Displacement and force chain distribution of the model after the ground stress equilibrium

As shown in the Table 4, the simulated vertical stresses are in good agreement with the theoretical values, with all relative errors falling within a small range. This verifies the accuracy of the model in simulating the self-weight stress field under a 20 g gravitational acceleration.

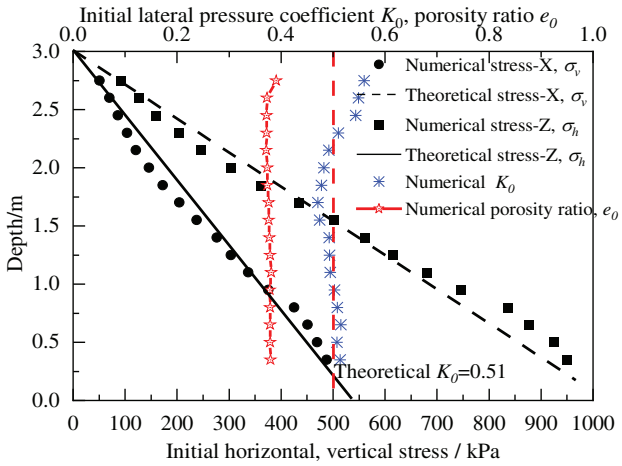


**Figure 15:** Distribution of stress state, porosity and lateral pressure coefficient

**Table 4:** Comparison of theoretical and simulated vertical stress at various depths

| Depth (m) | Theoretical vertical stress $\sigma_v$ (kPa) | Simulated vertical stress $\sigma_v$ (kPa) | Relative error (%) |
|---|---|---|---|
| 1.0 | 167 | 180 | +7.8% |
| 2.0 | 333 | 340 | +2.1% |
| 3.0 | 500 | 490 | −2.0% |

### *2.6 Excavation Process*

The final excavation depth of the foundation pit is 10 m, divided into 5 layers to reach the excavation depth, with each layer having a thickness of 2 m. In DEM, the excavation process of the foundation pit is simulated by progressively removing the sand particles layer by layer. After completing the excavation of one layer, the calculation is performed until the dissipation of unbalanced forces and the relative stability of particle displacements before proceeding to excavate the next layer. After the excavation is completed, in order to simulate the process of leveling the site after the excavation of the foundation pit in the project, particles are removed again in the range of 0–10 m so as to keep the bottom of the foundation pit flat. In the following text, 0 step represents the initial state, 1–5 step represents the excavation process from the first step to the fifth step, and 6 step represents the leveling process of the site.

## 3 Analysis of DEM Results

### *3.1 Stress Analysis of the Foundation Pit*

In order to study the variation of bottom stress with depth during the excavation process of the foundation pit, a set of measurement regions (measurement balls) is deployed within the pit. The measurement balls have a radius of 0.2 m and are spaced at intervals of 0.2 m, forming a total of 12 measurement circles, as shown in Fig. 16. During the staged excavation process of the cantilevered foundation pit, the overall stress distribution exhibits a characteristic of lower stress in the upper part and higher stress in the lower part. The stress in the bottom soil gradually decreases with each excavation, representing a stress release process caused by excavation. The top soil of the foundation

pit experiences a larger magnitude of unloading compared to the bottom soil, which is attributed to the greater stress release at the top during the excavation process. In addition, it can be seen that the stress reduction is not obvious during the excavation of steps 1 and 2, which is because the excavation amounts are small, resulting in a relatively small additional stress on the foundation. The changes are significant from steps 3 to 5, which is because the large excavation amounts of the foundation pit increases the stress release. From step 5 to 6, the stress remains relatively unchanged because, at this time, the excavation has ended, and the stress release at the bottom of the foundation pit has also ended. In summary, there is a stress release process at the bottom of the foundation pit during the excavation process, and the stress release at the bottom of the pit is most significant. Therefore, it can be seen that the discrete element method can accurately depict the process of changes in soil pressure at the bottom of the foundation pit.

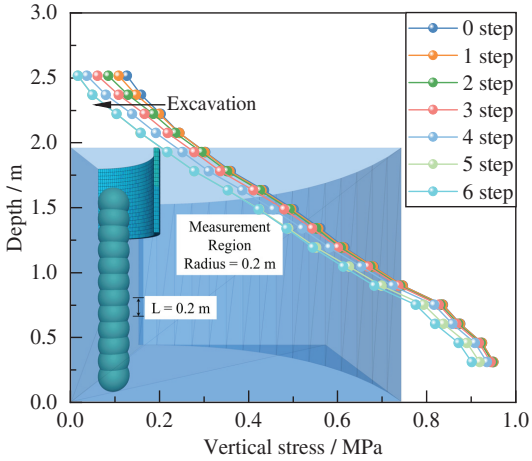


**Figure 16:** Changes in stress at the bottom of the foundation pit during the excavation process

### *3.2 Analysis for the Displacement Cloud Map of the Foundation Pit*

The displacement cloud map of the foundation pit is shown in Fig. 17. It can be seen from the figure that with the excavation of the foundation pit, large settlement first appears behind the wall and gradually develops inward. The maximum settlement value of the ground surface supported by the retaining wall occurs immediately behind the retaining wall, with a maximum settlement value of 3 cm. The farther away from the retaining wall, the smaller the settlement of the ground surface, which is consistent with the measured rules of a large number of cantilevered excavation foundation pits. At 2H away from the retaining wall, the settlement of the ground surface begins to converge and tends to zero. The settlement of the ground surface in this support method is consistent with the "triangle" settlement in the actual engineering rules, indicating that the deformation behavior of this type of foundation pit support in the discrete element simulation is feasible. After the excavation of step 3, obvious uplift appears at the bottom of the pit, and the uplift displacement is larger near the center of the foundation pit, with a maximum displacement of 4.4 cm. The soil behind the wall mainly shows settlement. From behind the retaining wall to the bottom of the excavation, the vertical displacement of the soil gradually transitions from settlement to upward uplift. The uplift of the soil at the bottom of the foundation pit is caused by the stress release resulting from excavation of the overlying soil. The maximum uplift of the soil at the center of the foundation pit is consistent with the actual engineering situation. In summary, a certain amount of uplift will occur during the step-by-step excavation of

the foundation pit, and each excavation level will exceed the uplift of the previous excavation level. Therefore, the over-excavation at the bottom during the excavation of the foundation pit cannot be ignored.

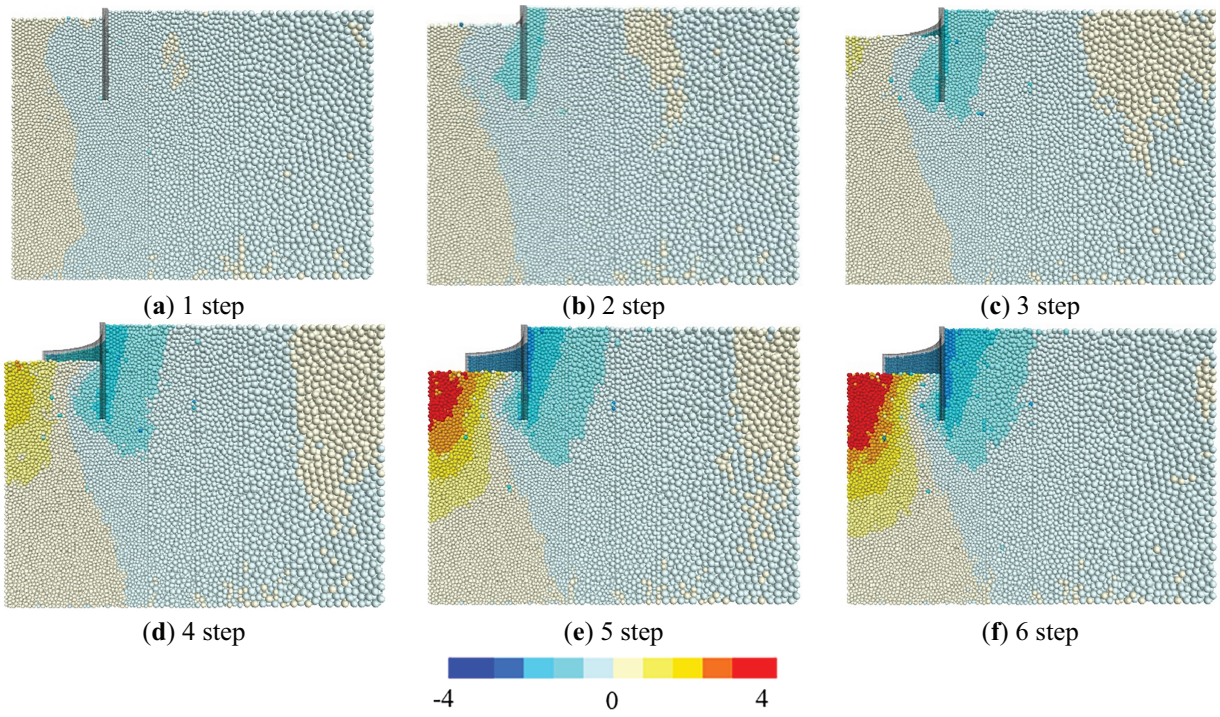


**Figure 17:** Displacement cloud map of foundation pit excavation (Unit: cm)

### *3.3 Vector Analysis for the Displacement of the Foundation Pit*

Fig. 18 shows the distribution of the velocity field of the sandy soil foundation after each excavation level is completed, which can be divided into the settlement area, the retaining wall influenced area, and the foundation pit uplift area according to the distribution of velocity vectors. During the excavation of step 1, the particles behind the wall settle, the particles in the influence area move upward, and the particles at the bottom of the pit move downward under the action of gravity. Therefore, during step 1, the particles mainly sink due to gravity. At step 2, the particles behind the wall continue to move downward, and the particles in the influence area show a vortex-like velocity vector under the joint action of stress release and gravity, while the particles at the bottom of the pit start to uplift. As the excavation continues, the range and velocity of the uplift area gradually increase, and the vortex-like vectors in the influenced area become more obvious, which is the result of the joint action of gravity and stress release. Finally, the velocity gradually decreases, and the foundation pit model tends to be in equilibrium. The influence depth of the uplift area at the bottom of the foundation pit is greater than the final depth of the burying depth of the retaining wall support. The use of retaining wall support has a poor effect on suppressing the plastic deformation of the soil, and there is a tendency for the soil outside the pit to move inward by passing the bottom of the retaining wall. The velocity vector at the center of the bottom of the pit is the largest, and its direction is vertical upward, indicating that the disturbance of particles in this area is the most obvious. Therefore, the uplift in this area during construction will cause over-excavation and make the soil looser.

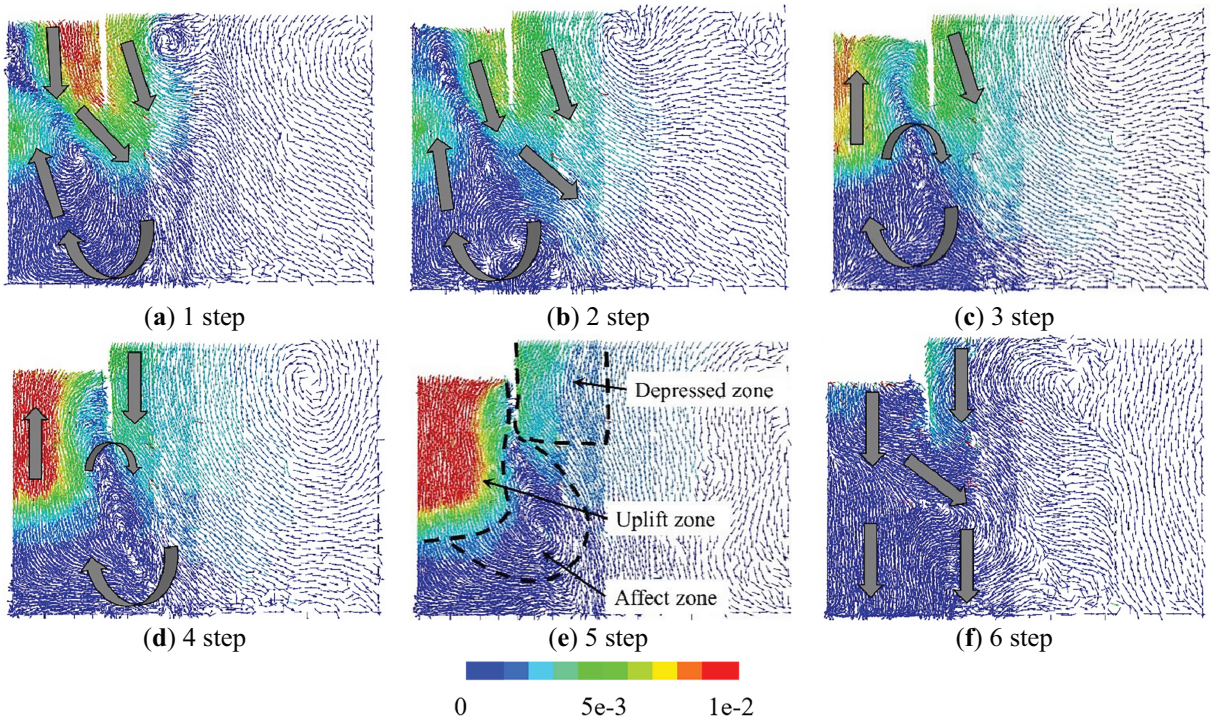


**Figure 18:** Vector analysis of displacement during foundation pit excavation (Unit: m/s)

### *3.4 Analysis for Porosity at the Bottom of the Foundation Pit*

A measuring circle was set at the bottom of the foundation pit to measure the changes in porosity during excavation, as shown in Fig. 19. It can be seen from the figure that the porosity gradually increases as the excavation progresses. This is because the foundation pit gradually uplifts after excavation, and the loose contact between particles increases the porosity. The increase in porosity is most significant at step 4 and 5, which also reflects the change in soil properties due to over-excavation of particles at the bottom of the foundation pit. At step 6, the porosity change is not significant due to the equilibrium of the model, which is consistent with the change in stress. Therefore, during foundation pit excavation, the porosity gradually increases due to the combined effects of the uplift of particles and over-excavation, which reduces the strength of the soil at the bottom of the pit. From a soil mechanics perspective, this increase in porosity directly corresponds to a decrease in soil stiffness and an increase in its compressibility. Consequently, this excavation-induced soil loosening heightens the potential for greater consolidation under subsequent superstructure loads, leading to significant post-construction settlement.

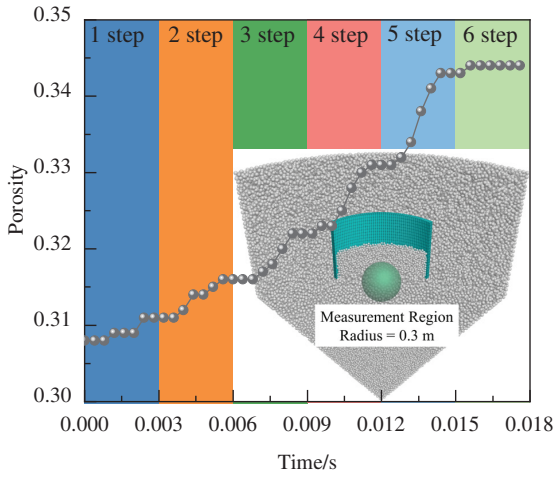


**Figure 19:** Curve of porosity variation at the bottom of the foundation pit with excavation

### *3.5 Analysis of Particle Displacement Paths*

To investigate the displacement paths of particles during foundation pit excavation, typical particles at three positions, located at the top of the foundation pit, the bottom of the retaining wall, and behind the retaining wall, were selected for study. As shown in Fig. 20a, the particles gradually uplifted as the excavation progressed, with the smallest displacement at step 1 and the largest displacement at steps 3–5, which is similar to the distribution of stress at the bottom of the foundation pit, indicating that the displacement of particles at the bottom of the foundation pit increased gradually with the release of stress. As shown in Fig. 20b, the particles gradually moved towards the downward slope as the foundation pit was excavated, indicating that the particles at the bottom of the retaining wall moved under the joint action of gravity and the pushing force of particles behind the wall during excavation. As shown in Fig. 20c, the particles gradually moved downward as the foundation pit was excavated, and the settlement of the foundation pit was relatively close with each excavation step.

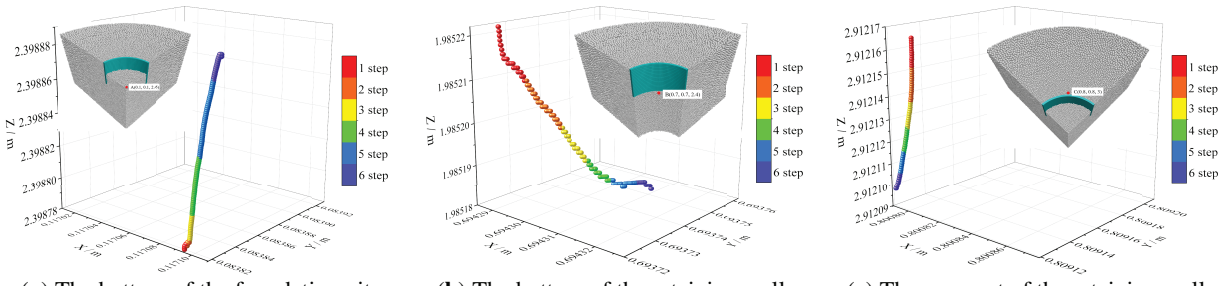


(**a**) The bottom of the foundation pit (**b**) The bottom of the retaining wall (**c**) The rear part of the retaining wall

**Figure 20:** Analysis of particle displacement paths at different locations

### *3.6 Analysis for Displacement of Monitoring Layers*

To further understand the spatial variation characteristics of the soil inside the embankment, a deformation monitoring layer was set in the model at a position of Z = 1.9 m. After the calculation was completed, the displacement information in the Z direction of the particles was recorded, and then the vertical displacement cloud map was interpolated, as shown in Fig. 21. It can be seen from

the figure that due to the constraint effect of the support structure, the uplift value near the foundation pit support structure is smaller than that in the middle of the foundation pit. As the foundation pit is excavated, the deformation of the monitoring layer gradually increases, with the most significant uplift occurring in the middle of the foundation pit. In summary, during the cantilever excavation of the foundation pit, the soil behind the retaining wall within a certain range mainly shows downward displacement towards the inside of the foundation pit, and the displacement of this part of the soil shows a triangular distribution. The soil in the center of the pit mainly shows upward uplift, and the displacement of the uplifted part at the bottom of the pit is greater than the settlement behind the wall.

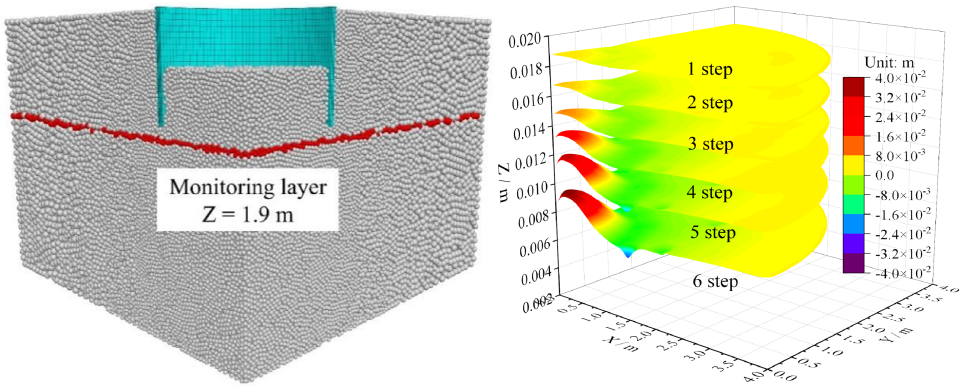


**Figure 21:** Changes in displacement of monitoring layers during foundation pit excavation

### *3.7 Force Chain Analysis*

One advantage of the discrete element method is its ability to obtain micro-scale data that is not easily measured in experiments, making it particularly suitable for analyzing particle skeleton structures and force chain networks. Fig. 22 shows the contact force chains between particles during the foundation pit excavation process. The color and thickness of the lines indicate the magnitude of the contact force; thicker lines represent greater forces. Overall, the force chain distribution is sparse in the upper part and dense in the lower part.

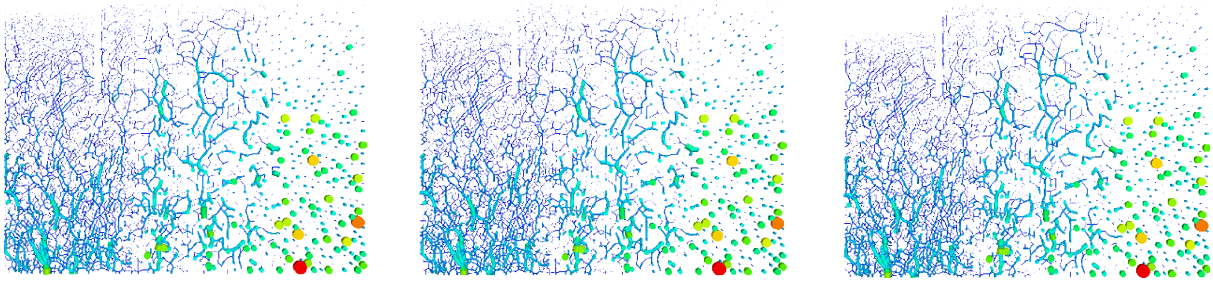

(**a**) 1 step (**b**) 2 step (**c**) 3 step

**Figure 22:** (Continued)

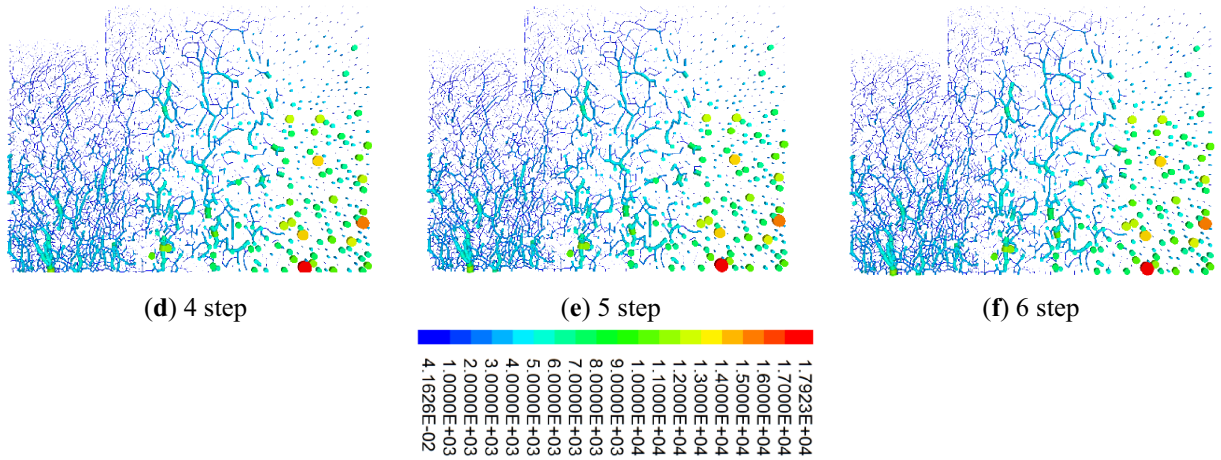


(**d**) 4 step (**e**) 5 step (**f**) 6 step

**Figure 22:** Force chain analysis during foundation pit excavation (Unit: N)

To provide a more quantitative assessment of the mechanical changes induced by excavation, we analyzed micro-parameters within a measurement region at the pit bottom. The analysis revealed a consistent decreasing trend in the average coordination number of the particles as the excavation progressed. This reduction in coordination number directly quantifies the decrease in particle contacts, confirming the loosening of the particle fabric. Regarding the magnitude of the contact forces, the maximum contact force observed throughout the process was approximately $1.8 \times 10^4$ N, located deep beneath the excavated pit bottom. However, despite these localized stress concentrations, the number of strong force chains (those carrying significant loads) in the pit bottom region diminished as a result of stress release. Therefore, the quantitative analysis of micro-parameters confirms that the force chains at the pit bottom become sparse due to stress release during the excavation process, reflecting a weakening of the soil's load-bearing skeleton. In contrast, although the soil behind the wall settled, the particle contacts did not change significantly, and thus the force chain network remained largely unaltered.

### *3.8 Analysis of Retaining Wall Displacement*

Fig. 23 shows the horizontal lateral displacement cloud map of the retaining wall at different excavation depths. Since the wall is completely elastic, the retaining wall tilts towards the pit in a combination of rigid body translation and rotation. During the cantilever layered excavation of the foundation pit, due to the unloading of the soil, the soil behind the wall acts as active earth pressure on the retaining wall, and the soil inside the foundation pit acts as passive earth pressure on the retaining wall. The larger displacements occur at the bottom of the retaining wall, indicating that the bottom of the retaining wall is significantly stressed under the action of soil pressure. When the foundation pit is excavated shallowly, the horizontal displacement of the retaining wall develops relatively slowly. As the depth of the foundation pit excavation increases, the displacement also increases, as can be seen from the lateral movement of the wall at the bottom. Overall, the bottom of the retaining wall gradually deforms outward under the action of soil pressure.

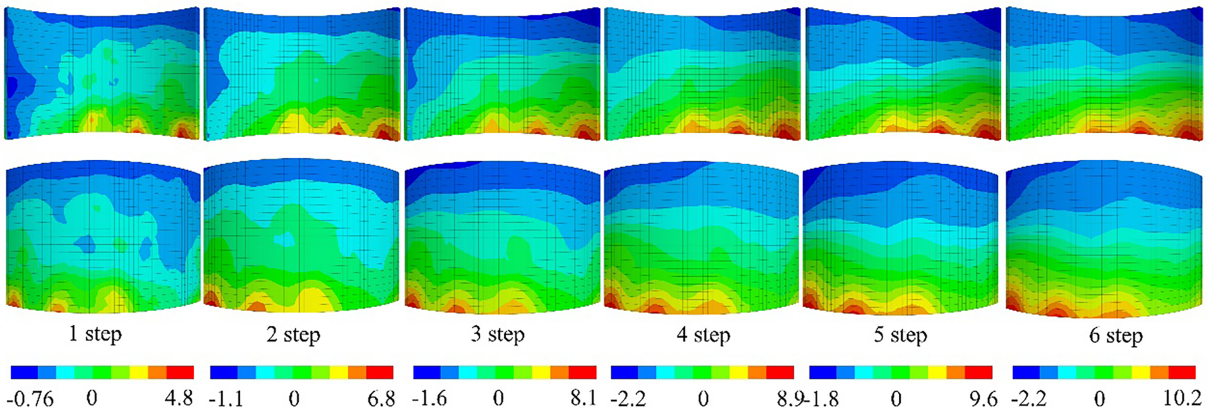


**Figure 23:** Lateral displacement cloud map of retaining wall during foundation pit excavation (Unit: mm)

Based on the discrete element method simulation, it can be concluded that the foundation pit mainly undergoes two processes during excavation: the excavation of the foundation pit and the construction leveling process. During the excavation phase of the foundation pit (steps 1–5), the soil at the bottom of the pit is uplifted, and due to the over-digging during construction, the strength of the soil is reduced. During the construction leveling phase (step 6), the final uplifted soil is excavated, causing further reduction in the strength of the soil at the bottom of the pit, especially at the center of the foundation pit. Therefore, for the compensated foundation that is subjected to structural loads after construction leveling, the same amount of settlement as the uplift during excavation will occur at the bottom of the pit.

## 4 Discussion

It is important to acknowledge the limitations and assumptions inherent in this numerical study. The simulated soil is an idealization of real sand; spherical particles were used, with a rolling resistance model to approximate the effects of angularity, and particle breakage was omitted due to the relatively low stress levels. The material parameters were also calibrated solely against triaxial compression tests.

Several numerical simplifications were adopted, primarily due to the high computational cost of 3D DEM. A formal convergence study for particle count and a mesh sensitivity analysis for the FEM wall were not performed; parameters were instead selected based on established best practices. The study is also based on a single, deterministic simulation, precluding an analysis of uncertainty. Furthermore, the excavation was modeled by instantaneous particle removal, an approach suitable for the cohesionless sand simulated but not for cohesive soils where consolidation is significant.

Finally, the study's scope is defined by the simulation of dry sand conditions without considering groundwater and the use of a specific model with a rigid wall and uniform soil. Consequently, the findings reveal fundamental mechanisms applicable to these conditions. Extending these conclusions to more complex scenarios-such as soft clays, flexible retaining structures, or saturated soils-will require developing more advanced models and validating them against physical tests and field case studies.

## 5 Conclusions

This study successfully simulated the cantilever excavation process of a foundation pit supported by a rigid retaining wall using the discrete element method, aiming to reveal the settlement mechanism of compensated foundations from a micro-mechanical perspective. The core novelty of this work lies in systematically revealing the intrinsic link from macroscopic phenomena to micro-mechanical mechanisms and elucidating the complete mechanical chain of events leading to the reduction of soil strength at the pit bottom. The main conclusions are as follows:

A Micro-Mechanical Mechanism of Soil Strength Degradation was Revealed: The study found that foundation pit excavation is not only a macroscopic process of stress release and basal heave, but also a mechanical process that leads to the progressive degradation of the soil's microstructure. This process manifests as a chain of events: stress release—upward particle movement—increased porosity—weakened contact forces and a sparser force chain network. This sequence of changes collectively causes a reduction in the bearing capacity of the foundation soil, with the most severe structural weakening occurring at the center of the pit where the heave is largest.

The Critical Impact of the "Site Leveling" Phase was Identified: This study specifically distinguishes between the effects of the "excavation phase" and the "site leveling phase". During the excavation phase, the soil loosens due to heave. The subsequent site leveling phase, where the uplifted soil is removed, acts as a second disturbance to the already weakened foundation soil, causing its strength to be further reduced. This is a critical step often overlooked in conventional analysis.

A Practical Engineering Countermeasure was Proposed: These findings have significant practical implications for understanding and mitigating excessive settlement in compensated foundations. The non-uniform heave pattern-largest in the middle and smaller at the sides-explains why theoretically compensated foundations still settle under structural loads, as the soil at the center is the loosest. Based on this mechanism, this study proposes the use of an inverted arch bottom plate structure as an effective countermeasure. The geometry of an inverted arch is opposite to the non-uniform heave profile, providing greater bending stiffness to resist the upward thrust of the central soil. This not only controls the non-uniform uplift but, more importantly, suppresses excessive soil loosening, thereby preserving the bearing capacity of the foundation soil and ultimately reducing long-term post-construction settlement.

**Acknowledgement:** This work was supported by the Guizhou Communications Polytechnic University. We gratefully acknowledge the Guangxi University for providing the necessary equipment for this study. We would like to thank Dr. Mei for his technical assistance during the experiments.

**Funding Statement:** This work had been supported by the Fund Project: the Scienc e and Technology Project of Guizhou Province (Qiankehe Fundamental QN [2025]420); Science and Technology Project of Guizhou Provincial Department of Transport (Grant No. 2025-121-015); High-Level Talent Research Startup Fund Project of Guizhou Communications Polytechnic University (KYQD2025004); the National Natural Science Foundation of China (52268054); Basic Research Project of Guizhou Provincial Department of Science and Technology, China (Grant No. ZK [2021]-290); Guizhou Province Science and Technology Plan Project, China (Grant No. GZSTCPT-CXTD [2021]008); Key Laboratory of High Performance Restoration Materials for Higher Education Construction Projects in Guizhou Province, China (Grant No. [2023]030).

**Author Contributions:** The authors confirm contribution to the paper as follows: study conception and design: Xiaoyong Zhang; data collection: Linhai Lv; analysis and interpretation of results: Meijuan

Xu; draft manuscript preparation: Guoxiong Mei. All authors reviewed the results and approved the final version of the manuscript.

**Availability of Data and Materials:** Due to the nature of this research, participants of this study did not agree for their data to be shared publicly, so supporting data is not available.

**Ethics Approval:** Not applicable.

**Conflicts of Interest:** The authors declare no conflicts of interest to report regarding the present study.

## References

1. Zeng CF, Zheng G, Zhou XF, Xue XL, Zhou HZ. Behaviours of wall and soil during pre-excavation dewatering under different foundation pit widths. Comput Geotech. 2019;115(5):103169. doi:10.1016/j.compgeo.2019.103169.
2. Goh ATC, Zhang RH, Wang W, Wang L, Liu HL, Zhang WG. Numerical study of the effects of groundwater drawdown on ground settlement for excavation in residual soils. Acta Geotech. 2020;15(5):1259–72. doi:10.1007/s11440-019-00843-5.
3. Meng FY, Chen RP, Xu Y, Wu K, Wu HN, Liu Y. Contributions to responses of existing tunnel subjected to nearby excavation: a review. Tunn Undergr Space Technol. 2022;119(6):104195. doi:10.1016/j.tust.2021.104195.
4. Ni P, Song L, Mei G, Zhao Y. Predicting excavation-induced settlement for embedded footing: case study. Int J Geomech. 2018;18(4):05018001. doi:10.1061/(asce)gm.1943-5622.0001107.
5. Lyu HM, Shen SL, Zhou A, Yang J. Perspectives for flood risk assessment and management for mega-city metro system. Tunn Undergr Space Technol. 2019;84(1):31–44. doi:10.1016/j.tust.2018.10.019.
6. Sales MM, Small JC, Poulos HG. Compensated piled rafts in clayey soils: behaviour, measurements, and predictions. Can Geotech J. 2010;47(3):327–45. doi:10.1139/t09-106.
7. Tang Y, Zhao X. 121-story Shanghai Center Tower foundation re-analysis using a compensated pile foundation theory. Struct Des Tall Spec Build. 2014;23(11):854–79. doi:10.1002/tal.1087.
8. Tan Y, Li M. Measured performance of a 26 m deep top-down excavation in downtown Shanghai. Can Geotech J. 2011;48(5):704–19. doi:10.1139/t10-100.
9. Tan Y, Wei B. Observed behaviors of a long and deep excavation constructed by cut-and-cover technique in Shanghai soft clay. J Geotech Geoenviron Eng. 2012;138(1):69–88. doi:10.1061/(asce)gt.1943-5606.0000553.
10. Shahriar MA, Sivakugan N, Das BM, Urquhart A, Tapiolas M. Water table correction factors for settlements of shallow foundations in granular soils. Int J Geomech. 2015;15(1):06014015. doi:10.1061/(asce)gm.1943-5622.0000391.
11. Jafarian Y, Haddad A, Mehrzad B. Load-settlement mechanism of shallow foundations rested on saturated sand with upward seepage. Int J Geomech. 2017;17(3):04016076. doi:10.1061/(asce)gm.1943-5622.0000777.
12. Cundall PA, Strack ODL. A discrete numerical model for granular assemblies. Géotechnique. 1979;29(1):47–65. doi:10.1680/geot.1979.29.1.47.
13. Nicot F, Sibille L, Donze F, Darve F. From microscopic to macroscopic second-order work in granular assemblies. Mech Mater. 2007;39(7):664–84. doi:10.1016/j.mechmat.2006.10.003.
14. Liu T, Zhang C, Li W, Tu S, Wang L, Jin Z. Face failure mechanism of fault tunnels under high-temperature and high-pressure conditions using the discrete element method. Comput Geotech. 2025;179(4):107059. doi:10.1016/j.compgeo.2025.107059.
15. Li X, Yu HS, Li XS. A virtual experiment technique on the elementary behaviour of granular materials with discrete element method. Int J Numer Anal Meth Geomech. 2013;37(1):75–96. doi:10.1002/nag.1086.

16. Meier HA, Schlemmer M, Wagner C, Kerren A, Hagen H, Kuhl E, et al. Visualization of particle interactions in granular media. IEEE Trans Visual Comput Graphics. 2008;14(5):1110–25. doi:10.1109/tvcg.2008.65.
17. Liu T, Zhou J, Liang L, Zhao Y, Cao D. Investigation of effect of stones on lunar regolith drilling using DEM. Comput Geotech. 2021;131(1):103958. doi:10.1016/j.compgeo.2020.103958.
18. Lo Y. Simulation of soil mechanical behaviors using discrete element method based on particle flow code and it application. Hangzhou, China: Zhejiang University; 2007. (In Chinese).
19. Peng S. Macro-scale and meso-scale study on failure mechanism of sand retaining wall. Shanghai, China: Tongji University; 2007. (In Chinese).
20. Jia M, Wang L, Zhou J. Simulation of soil deformation due to pit excavation with particle flow code. J TongJi Univ Nat Sci. 2009;37(5):612–17. (In Chinese).
21. Widuliński Ł, Tejchman J, Kozicki J, Leśniewska D. Discrete simulations of shear zone patterning in sand in earth pressure problems of a retaining wall. Int J Solids Struct. 2011;48(7–8):1191–209. doi:10.1016/j.ijsolstr.2011.01.005.
22. Jiang M, He J, Wang J, Liu F, Zhang W. Distinct simulation of earth pressure against a rigid retaining wall considering inter-particle rolling resistance in sandy backfill. Granul Matter. 2014;16(5):797–814. doi:10.1007/s10035-014-0515-3.
23. Nakashima H, Oida A. Algorithm and implementation of soil-tire contact analysis code based on dynamic FE-DE method. J Terramech. 2004;41(2–3):127–37. doi:10.1016/j.jterra.2004.02.002.
24. Li Y, Gan J, Zhang G, Liu Z, Guo G, Guo B, et al. Research on strata movement control in deep composite lithologic gangue backfill mining of super-thick and weak cementation overburden based on PFC-FLAC coupling simulation. Adv Civ Eng. 2025;2025(1):6650989. doi:10.1155/adce/6650989.
25. Park T, Ahmed B, Voyiadjis GZ. A review of continuum damage and plasticity in concrete: part I—Theoretical framework. Int J Damage Mech. 2022;31(6):901–54. doi:10.1177/10567895211068174.
26. Sun J, Li XA, Li J, Zhang J, Zhang Y. Numerical investigation of characteristics and mechanism of tunnel erosion of loess with coupled CFD and DEM method. CATENA. 2023;222:106729. doi:10.1016/j.catena.2022.106729.
27. Zeng Q, Yang X, Tu J, Wei H, Yuan X, Cai C, et al. Investigation on rock-breaking and debris transport of high-pressure water jet drilling using the discrete element method (DEM). Geoenergy Sci Eng. 2025;249(2):213750. doi:10.1016/j.geoen.2025.213750.
28. Yoo C, Lee D. Deep excavation-induced ground surface movement characteristics—A numerical investigation. Comput Geotech. 2008;35(2):231–52. doi:10.1016/j.compgeo.2007.05.002.
29. Rechea C, Levasseur S, Finno R. Inverse analysis techniques for parameter identification in simulation of excavation support systems. Comput Geotech. 2008;35(3):331–45. doi:10.1016/j.compgeo.2007.08.008.
30. Zhang M, Yao Y, Pei H, Zheng J. A new isotropic hardening constitutive model based on reference compression curve. Comput Geotech. 2021;138(2):104337. doi:10.1016/j.compgeo.2021.104337.
31. Shi D, Yang Y, Deng Y, Xue J. DEM modelling of screw pile penetration in loose granular assemblies considering the effect of drilling velocity ratio. Granul Matter. 2019;21(3):74. doi:10.1007/s10035-019-0933-3.
32. Iwashita K, Oda M. Rolling resistance at contacts in simulation of shear band development by DEM. J Eng Mech. 1998;124(3):285–92. doi:10.1061/(asce)0733-9399(1998)124:.
33. Jiang MJ, He J, Liu F. Distinct element simulation of passive earth pressure against a translating rigid wall using a rolling resistance contact model. Rock Soil Mech. 2012;33(9):2788–95. (In Chinese). doi:10.16285/j.rsm.2012.09.016.
34. Mohamed A, Gutierrez M. Comprehensive study of the effects of rolling resistance on the stress-strain and strain localization behavior of granular materials. Granul Matter. 2010;12(5):527–41. doi:10.1007/s10035-010-0211-x.

35. Zhang X, Wang T, Zhao C, Jiang M, Xu M, Mei G. Supporting mechanism of rigid-flexible composition retaining structure in sand ground using discrete element method. Comput Geotech. 2022;151(3):104967. doi:10.1016/j.compgeo.2022.104967.
36. Itasca Consulting Group. PFC2D (Particle flow code in 2 dimensions) (Version 5.1). Minneapolis, MN, USA: Itasca Consulting Group Inc.; 2004.
37. Chen Q, Li Z, Dai Z, Wang X, Zhang C, Zhang X. Mechanical behavior and particle crushing of irregular granular material under high pressure using discrete element method. Sci Rep. 2023;13(1):7843. doi:10.1038/s41598-023-35022-w.
38. Zhao Y, Konietzky H, Herbst M. Damage evolution of coal with inclusions under triaxial compression. Rock Mech Rock Eng. 2021;54(10):5319–36. doi:10.1007/s00603-021-02436-9.
39. Tan X, Hu Z, Cao M, Chen C. 3D discrete element simulation of a geotextile-encased stone column under uniaxial compression testing. Comput Geotech. 2020;126(5):103769. doi:10.1016/j.compgeo.2020.103769.
40. Zhang X, Jiang M, Yang J, Zhao C, Mei G. The macroscopic and mesoscopic study on strengthening mechanisms of the single pile with raft under pile-soil-raft combined interaction. Comput Geotech. 2022;144(4):104630. doi:10.1016/j.compgeo.2021.104630.
41. McDowell GR, Falagush O, Yu HS. A particle refinement method for simulating DEM of cone penetration testing in granular materials. Géotechnique Lett. 2012;2(3):141–7. doi:10.1680/geolett.12.00036.
42. Deng Y, Yang Y, Shi D, Liu W. Refinement and application of variable particle-size methods in 3D discrete element modelling for large-scale problems. Chin J Geotech Eng. 2017;39(1):62–70. (In Chinese).
43. Chen Y, Deng A, Wang A, Sun H. Performance of screw-shaft pile in sand: model test and DEM simulation. Comput Geotech. 2018;104(9):118–30. doi:10.1016/j.compgeo.2018.08.013.
44. Peng Y, Ding X, Yin ZY, Wang P. Micromechanical analysis of the particle corner breakage effect on pile penetration resistance and formation of breakage zones in coral sand. Ocean Eng. 2022;259(3):111859. doi:10.1016/j.oceaneng.2022.111859.
45. Bryant SK, Take WA, Bowman ET, Millen MDL. Physical and numerical modelling of dry granular flows under Coriolis conditions. Géotechnique. 2015;65(3):188–200. doi:10.1680/geot.13.p.208.
46. Cabrera MA, Leonardi A, Peng C. Granular flow simulation in a centrifugal acceleration field. Géotechnique. 2020;70(10):894–905. doi:10.1680/jgeot.18.p.260.
47. Stopka G, Kotwica K. Estimation of excavation forces in conditions of a complex cutting trajectory with asymmetrical disc tools in DEM method. Tunn Undergr Space Technol. 2023;142(1):105439. doi:10.1016/j.tust.2023.105439.